

# **Fast and accurate amyloid brain PET quantification without MRI using deep neural networks**

Seung Kwan Kang<sup>1,2</sup>, Daewoon Kim<sup>3,6</sup>, Seong A Shin<sup>1</sup>, Yu Kyeong Kim<sup>4,5</sup>, Hongyoon Choi<sup>2,4</sup>, and Jae Sung Lee<sup>1,2,3,4,6</sup>

<sup>1</sup>Brightonix Imaging Inc., Seoul, Korea

<sup>2</sup>Institute of Radiation Medicine, Medical Research Center, Seoul National University College of Medicine, Seoul, Korea

<sup>3</sup>Interdisciplinary Program of Bioengineering, Seoul National University, Seoul, Korea

<sup>4</sup>Department of Nuclear Medicine, Seoul National University College of Medicine, Seoul, Korea

<sup>5</sup>Department of Nuclear Medicine, Seoul Metropolitan Government Seoul National University Boramae Medical Center

<sup>6</sup>Artificial Intelligence Institute, Seoul National University, Seoul, Korea

## **Name and address for correspondence and reprint requests:**

Jae Sung Lee, PhD

Department of Nuclear Medicine, Seoul National University College of Medicine, 103 Daehak-ro, Jongno-gu, Seoul 03080, Korea.

Phone: +82-2-2072-2938; E-mail: [jaes@snu.ac.kr](mailto:jaes@snu.ac.kr)

**Name and address of the first author:**

Seung Kwan Kang, PhD

Brightonix Imaging Inc., Seongsu-yeok SK V1 Tower, 25 Yeonmujang 5ga-gil, Seongdong-gu, Seoul 04782, Republic of Korea.

Phone: +82-2-766-8745; E-mail: [kevin.kang@brtnx.com](mailto:kevin.kang@brtnx.com)

Total number of words in the manuscript: 4,815

**Running title:** Spatial normalization with deep learning

**Immediate Open Access:** Creative Commons Attribution 4.0 International License (CC BY) allows users to share and adapt with attribution, excluding materials credited to previous publications.

License: <https://creativecommons.org/licenses/by/4.0/>.

Details: <https://jnm.snmjournals.org/page/permissions>.



## Abstract

This paper proposes a novel method for the automatic quantification of amyloid positron emission tomography (PET) using the deep learning (DL)-based spatial normalization (SN) of PET images, which does not require magnetic resonance imaging (MRI) or computed tomography images of the same patient. The accuracy of the method was evaluated for three different amyloid PET radiotracers compared to MRI-parcellation-based PET quantification using FreeSurfer.

**Methods:** A deep neural network model used for the SN of amyloid PET images was trained using 994 multicenter amyloid PET images (367  $^{18}\text{F}$ -Flutemetamol and 627  $^{18}\text{F}$ -Florbetaben) and the corresponding 3D MRIs of patients with Alzheimer’s disease or mild cognitive impairment, and cognitively normal subjects. For comparison, PET SN was also conducted using the SPM12 program (SPM-based SN). The accuracy of DL- and SPM-based SN and standardized uptake value ratio (SUVR) quantification relative to the FreeSurfer-based estimation in individual brain spaces was evaluated using 148 other amyloid PET images (64  $^{18}\text{F}$ -Flutemetamol and 84  $^{18}\text{F}$ -Florbetaben). Additional external validation was performed using an unseen independent external dataset (30  $^{18}\text{F}$ -Flutemetamol, 67  $^{18}\text{F}$ -Florbetaben, and 39  $^{18}\text{F}$ -Florbetapir).

**Results:** Quantification results using the proposed DL-based method showed stronger correlations with the FreeSurfer estimates than SPM-based SN using MRI did. For example, the slope,  $y$ -intercept and  $R^2$  values between SPM and FreeSurfer for the global cortex were 0.869, 0.113, and 0.946, respectively. In contrast, the slope,  $y$ -intercept, and  $R^2$  values between the proposed DL-based method and FreeSurfer were 1.019, -0.016, and 0.986, respectively. The external validation study also demonstrated better performance of the proposed method without MR images than that of SPM with MRI. In most brain regions, the proposed method outperformed the SPM SN in terms of linear regression parameters and intraclass correlation coefficients.

**Conclusion:** We evaluated a novel DL-based SN method, which allows quantitative analysis of amyloid

brain PET images without structural MRI. The quantification results using the proposed method showed a strong correlation with MRI-parcellation-based quantification using FreeSurfer for all clinical amyloid radiotracers. Therefore, the proposed method will be useful for investigating Alzheimer's disease and related brain disorders using amyloid PET scans.

**Key words:** amyloid PET, spatial normalization, deep learning, quantification

## Introduction

Owing to the nature of brain diseases, the pathological condition of the brain should be evaluated in a non-invasive manner. Positron emission tomography (PET) is a useful imaging tool for assessing the functional and molecular status of the brain (1,2). The application of brain PET imaging in the diagnosis and treatment of degenerative brain diseases is widely increasing (3-5). In Alzheimer's dementia (AD), the most common degenerative brain disease, brain deposition of fibrillar amyloid beta plaques is a neuropathological hallmark for diagnosis. Therefore, amyloid PET has significantly contributed to the diagnosis and treatment of AD.

The visual assessment of PET images by nuclear medicine physicians or radiologists is the standard method for clinical neuroimaging interpretation. Nevertheless, quantitative and statistical analyses of PET images are widely used in brain disease research (1,2,6-9). This is because such analyses provide useful information for the objective interpretation of the PET images of individual patients. The most prevalent method of quantitative image analysis is evaluating the regional uptake of radiotracers by manually drawing the region-of-interest or volume-of-interest (VOI) on individual brain PET images. Another common method for brain PET image analysis is voxel-wise statistical analysis, which is based on the spatial normalization (SN) of images (10-12). Furthermore, brain PET SN allows the use of predefined VOIs, which is a suitable alternative to laborious and time-consuming manual VOI drawing (13-19).

Monoclonal antibodies such as aducanumab and donanemab are emerging as treatment drugs for AD, which target aggregated amyloid beta to reduce its buildup in the brain (20,21). Therefore, the importance of quantification methods for amyloid brain PET images with high objectivity, accuracy, and reproducibility is increasing. Although voxel-wise statistical analysis and predefined-VOI-based automated anatomical labeling are objective and efficient methods for amyloid brain PET image analysis, their reliability primarily depends on the accuracy of the SN procedure. However, accurate amyloid PET SN without the

complementary use of anatomical images, such as magnetic resonance imaging (MRI) or computed tomography (CT), is technically challenging owing to the large discrepancy in amyloid deposit patterns between normal and abnormal cases (22-24). Additionally, severe cerebral atrophy and hydrocephalus, which are frequently observed in older patients, complicate SN. Previously, we proposed two deep-learning-based amyloid PET SN methods that did not require matched MRI or CT data (25,26). In one of these approaches (25), we used a generative adversarial network (GAN) to generate pseudo-MRI data from amyloid PET and applied spatial transformation parameters, obtained by performing SNs of pseudo-MRIs on the MRI template, to amyloid PET images. In the second approach (26), we used deep neural networks to generate adaptive PET templates for individual amyloid PET images and performed SNs of amyloid PET images using individual adaptive templates. Both approaches showed a strong correlation of regional standardized uptake value ratio (SUVR) relative to cerebellar activity with the matched MRI-based PET SN and outperformed the MRI-less SN with the average amyloid PET template. However, these methods have the following limitations: First, the process of generating a pseudo-MRI or adaptive template using deep neural networks and the SN process are separated. Second, we used the SN algorithm provided by the Statistical Parametric Mapping (SPM; University of College London, UK) software, which iteratively applies image registration and segmentation algorithms (27). Therefore, the accuracy and speed of the entire SN pipeline depend on the SN performance and computation time of the SPM. These limitations undermine the advantage of not requiring matched MRI for amyloid PET SN in both approaches.

Therefore, in this study, we developed a novel MRI-less amyloid PET SN method that allows the one-step generation of spatially normalized PET images using cascaded deep neural networks that estimate linear and nonlinear SN parameters from individual amyloid PET images. Furthermore, we evaluated the accuracy of the proposed method for three different amyloid PET radiotracers compared to MRI parcellation-based PET quantification using FreeSurfer (28), which has shown a strong correlation with a manual-drawing method in cortical thickness and volume measurement (29-31) and regional amyloid load

estimation (32,33) but requires a significantly longer computation time (approximately 8 h).

## Materials and Methods

### *Datasets*

To train and test the deep neural network (DNN) model for PET SN, we utilized an open-access dataset provided by the National Information Society Agency (NIA, <https://aihub.or.kr/>). This “internal dataset” comprised pairs of multicenter amyloid PET scans ( $^{18}\text{F}$ -Florbetaben or  $^{18}\text{F}$ -Flutemetamol) and structural T1-weighted 3D MRI scans of patients with AD or mild cognitive impairment (MCI) and cognitively normal subjects. The image data were acquired from six university hospitals in South Korea. The demographic information and clinical diagnoses of the training and test sets are summarized in **Table 1**. Public Institutional Bioethics Committee designated by the Ministry of Health and Welfare of South Korea approved the retrospective use of the scan data and waiver of the need for informed consent.

Furthermore, the trained network was evaluated using an “external dataset” obtained from the Global Alzheimer’s Association Interactive Network (GAAIN; <http://www.gaain.org/centiloid-project>). The trained network was tested for three different FDA-approved amyloid tracers:  $^{18}\text{F}$ -Florbetaben,  $^{18}\text{F}$ -Flutemetamol, and  $^{18}\text{F}$ -Florbetapir. Originally, this dataset, comprising young controls and elderly subjects, was acquired for the Centiloid calibration of each tracer (34-36). The demographic information is summarized in **Table 2**.

### *Network Model*

The proposed DNN model, comprising cascaded U-Nets (37) takes an affine-registered amyloid PET image as an input and generates local displacement fields for nonlinear registration (**Supplemental Fig. 1**). The generated displacement fields were then applied to the co-registered MRI in the training phase, and the

cross-correlation loss between the spatially normalized MRI and the T1 template (individual MNI152) was minimized by error back propagation. Additionally, the gray matter (GM) segment of each MRI was utilized to improve the performance of the trained network and deformed using the same displacement fields as shown in **Supplemental Fig. 1**. Dice loss was calculated between the deformed GM segment and the GM of the MNI152 template, which was minimized along with the cross-correlation loss. On-the-fly data augmentation was applied when training the network model to prevent parameter overfitting. Spatially normalized PET images were not required in the training phase, and only PET images in individual spaces were used to create deformation fields. When the DNN model was trained, only PET images in an individual space were fed into the DNN model to generate SN images in the template space (**Fig. 1A**).

#### *Quantification of Amyloid Load*

SN was conducted using the SPM12 program (<https://www.fil.ion.ucl.ac.uk/spm>) for comparison (**Fig. 1B**). Using the SPM12 program, PET and MRI pairs were co-registered, and the MRI images were spatially normalized. The MRI SN was performed using a unified segmentation method that utilizes tissue probability maps as deformable spatial priors for regularization of the non-linear deformations (27). The PET images were then spatially normalized using the deformation fields estimated from the paired MRI.

Using the VOIs predefined in the template space, regional PET counts were extracted from spatially normalized images using DNN or SPM. The predefined VOIs were generated by applying automatic MRI parcellation using FreeSurfer 7.1.0 software (Martinos Center for Biomedical Imaging, Charlestown, Massachusetts, USA) to MNI template (38,39). The cortical and subcortical structures segmented and parcellated by FreeSurfer were grouped into six composite VOIs: global cerebral cortex, frontal lobe, posterior cingulate cortex and precuneus, lateral parietal, lateral temporal, and medial temporal. The counts of the VOIs were then divided by the counts of the cerebellar gray matter to calculate SUVR.

As a reference, SUVR values in individual brain spaces were estimated using T1-weighted 3D MR



images and FreeSurfer (**Fig. 1C**). The results of the FreeSurfer segmentation of MR images were visually inspected by a neuroscience expert to ensure quality assurance in all datasets. About 10% of the datasets were excluded due to incomplete cortex segmentation or cessation of FreeSurfer program. Failure cases were higher in elderly subjects (young controls: 8.7%, elderly: 10.5%). Finally, the six composite VOIs were applied to the co-registered amyloid brain PET images to calculate SUVR. FreeSurfer SUVR estimated in individual space was regarded as ground truth because FreeSurfer and manual-drawing approaches achieved nearly identical estimates of amyloid load (32).

### *Statistical Analysis*

The correlation between SN-based approaches (DNN or SPM) and the FreeSurfer approach was evaluated using Pearson's correlation. Furthermore, we performed a Bland–Altman analysis on the SUVR. Additionally, intraclass correlation coefficients (ICCs) were calculated to assess the consistency of the quantification results.

## **Results**

After network training, the proposed DNN method successfully generated displacement fields for SN and achieved accurate spatially normalized PET images, as shown in **Figure 2 and Supplemental Figure 2**. However, the SPM12 SN was not sufficiently accurate for patients with a severe ventricular enlargement (**Fig. 2 and Supplemental Fig. 2**); nonetheless, the ventricular enlargement did not degrade the performance of the proposed method. **Figure 2 and Supplemental Figure 2** show a representative amyloid-positive case and an amyloid-negative case with a global SUVR of 1.889 (73-year-old female; diagnosis: AD; tracer: $^{18}\text{F}$ -Florbetaben) and 1.318 (80-year-old female; diagnosis: cognitively normal; tracer: $^{18}\text{F}$ -Florbetaben), respectively.

The proposed DNN method is also robust in the SN of lesioned brains. **Figure 3 and Supplemental Figure 3** show the SN result of a patient (84-year-old female; tracer:  $^{18}\text{F}$ -Florbetaben) with a chronic stroke lesion using the proposed method, thereby enabling accurate SN with no shrinkage in lesion volume.

Additionally, the proposed DNN method showed a better correlation with the FreeSurfer approach compared to SPM12 SN in all three tested radiotracers and most of the tested VOIs (**Figs. 4-7 and Tables 3-6**). Furthermore, the proposed method yielded higher ICC results than SPM12 in almost all comparisons (**Tables 3-6**). Moreover, the proposed method showed a lower bias in SUVR estimation in the Bland–Altman analysis (**Supplemental Figs. 4-7**). No remarkable differences were observed between the internal and external validation results. Although the  $^{18}\text{F}$ -Florbetapir data was not used in the DNN training, the proposed method showed no performance degradation for the external  $^{18}\text{F}$ -Florbetapir dataset. The results of separate analysis for amyloid positive and negative cases which were divided by global SUVR of 1.5 are summarized in **Supplemental Tables 1-4**.

The computation time required for PET SN using the proposed method was approximately 1 s. Conversely, SPM required > 60 s for the batch operation that included the co-registration between PET and MRI, spatial normalization parameter estimation from MRI, and writing the spatially normalized PET image. FreeSurfer required approximately 8 h for automatic MRI parcellation.

## Discussion

In this study, we developed a fast amyloid brain PET SN method based on DNNs to overcome the limitations of existing approaches based on paired anatomical images or patient-specific templates (25,26,32). Furthermore, we assessed the correlation and measurement consistency between the proposed method and FreeSurfer-based SUVR quantification, which showed a strong correlation with the manual VOI approach (32). In terms of correlation and consistency with the FreeSurfer-based approach, the DNN-based PET SN method outperformed MRI-based PET SN that was conducted using the co-registration and SN routines of SPM12, which is one of the most widely used pipelines for amyloid brain PET research.

The DNN model trained in this study allowed a robust SN of amyloid PET images without MRI. The superiority of the SN performance of the proposed method compared to that of SPM SN using MRI was most pronounced in cases with hydrocephalus, as shown in **Figure 2 and Supplemental Figure 2**. The DNN model trained using nearly 1,000 datasets with on-the-fly data augmentation was able to generate SN PET images that were morphologically consistent with the standard MRI template. Although the DNN model was trained using a Korean dataset, no performance difference was observed when it was applied to external datasets obtained from other countries. Accurate spatial normalization of the lesioned brain was also possible, as shown in **Figure 3**, without shrinkage of the lesion volume, which is frequently observed in conventional SN approaches (40). However, despite the use of MRI, SPM SN could not compensate for the large morphological differences between the input images and the template. In the SN algorithm used in SPM, the images are deformed by the linear combination of thousand cosine transform bases, which allowed only a limited amount of image deformation.

A potential alternative approach to the proposed method is generating spatially normalized amyloid PET images directly from individual PET inputs using DNNs. This method is faster compared to the proposed method considering it directly conducts SN without generating explicit deformation fields. However, direct

SN methods are more susceptible to the perturbation of input images owing to noise. Therefore, it is difficult to ensure the maintenance of regional count rate concentrations after the direct SN of brain PET images. However, the DNN model used in the proposed method does not directly provide the image intensity of SN images. The intensities were calculated by interpolating neighbor voxel values using DNN-generated deformation fields, which reduced the risk of erroneous intensity mapping by the SN. In addition, the DNN model trained for deformation field generation using amyloid PET images can be utilized for transfer learning on other radiotracers with small data sets available. Our preliminary (unpublished) study on  $^{18}\text{F}$ -Flortaucipir shows that the transfer learning allows for highly accurate quantification of  $^{18}\text{F}$ -Flortaucipir brain PET using the proposed method.

The proposed fast and reliable deep-learning-based spatial normalization of amyloid PET images can be potentially used to improve the inter-reader agreement and the confidence of amyloid PET interpretation. In our previous study (41), when visual amyloid PET interpretation was supported by a deep learning model that directly estimated regional SUVR from input images (42), the inter-reader agreement (Fleiss kappa coefficient) and confidence score increased from 0.46 to 0.76 and from 1.27 to 1.66, respectively. The method proposed herein requires a longer computation time for regional SUVR calculation than the direct end-to-end SUVR estimation, mainly because of the voxel-by-voxel multiplication of SN results and the predefined brain atlas. However, the reliability of the amyloid burden estimation based on the proposed method is higher, considering the proposed method allows the visual confirmation of SN results and the exclusion of cases with erroneous SNs. Furthermore, accurate automatic quantification of amyloid burden can be used in longitudinal follow-up studies in patients with AD and MCI. Several dementia treatment drugs based on the amyloid hypothesis are now emerging, and amyloid PET scans are important for monitoring the efficacy of treatments. The proposed method will enable an objective measurement of drug-induced amyloid clearance without requiring additional 3D structural MRI.

## **Conclusion**

We evaluated a novel deep learning-based SN method, which allows quantitative analysis of amyloid brain PET images without structural MRI. The quantification results using the proposed method showed a strong correlation with MRI-parcellation-based quantification using FreeSurfer for all clinical amyloid radiotracers. Therefore, the proposed method will be useful for investigating Alzheimer's disease and related brain disorders using amyloid PET scans.

## **Financial Disclosure**

This research was supported by Seoul R&BD Program (No. BT200151) through the Seoul Business Agency (SBA) funded by The Seoul Metropolitan Government.

## **Disclaimer**

The authors declare no potential conflicts of interest relevant to this article.

**Key Points**

**Question:** Is the quantification of amyloid PET images without MRI feasible?

**Pertinent Findings:** A method based on deep learning allowed fast and reliable amyloid PET spatial normalization and quantification without MRI.

**Implications for Patient Care:** The proposed method will be useful for interpreting amyloid PET scans in Alzheimer's disease and related brain disorders.

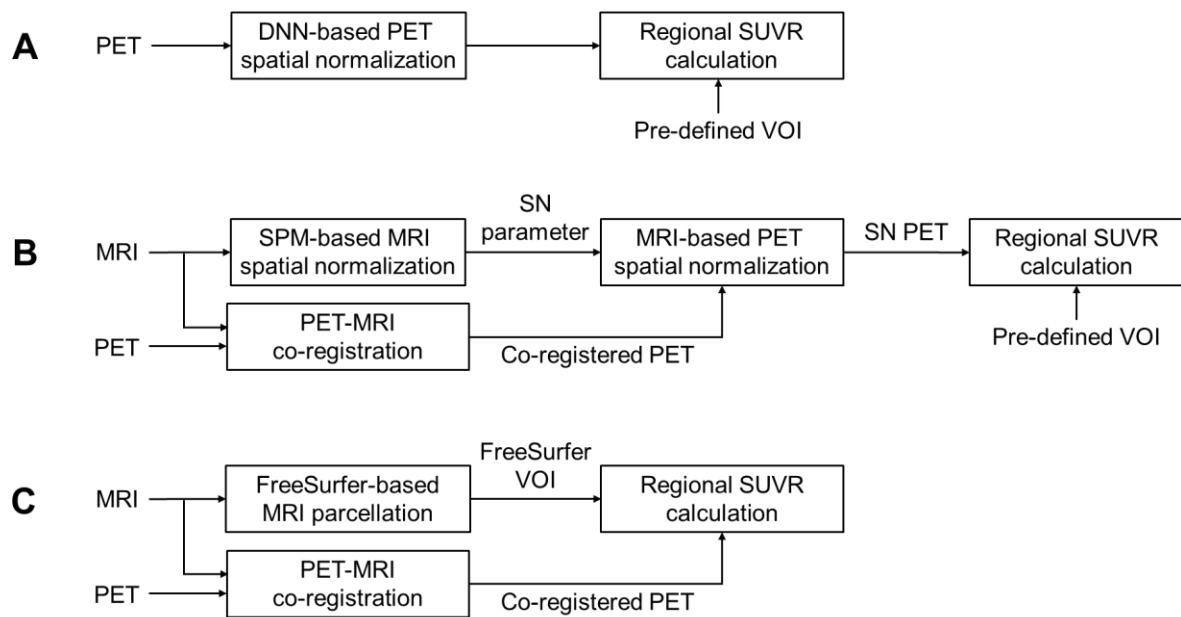


**FIGURE 1.** Three approaches used to estimate regional SUVR from amyloid PET images are compared in this study. (A) Deep neural network (DNN) based PET spatial normalization, (B) PET-MRI co-registration and MRI-based PET spatial normalization using SPM, and (C) PET-MRI co-registration and MRI parcellation using FreeSurfer.

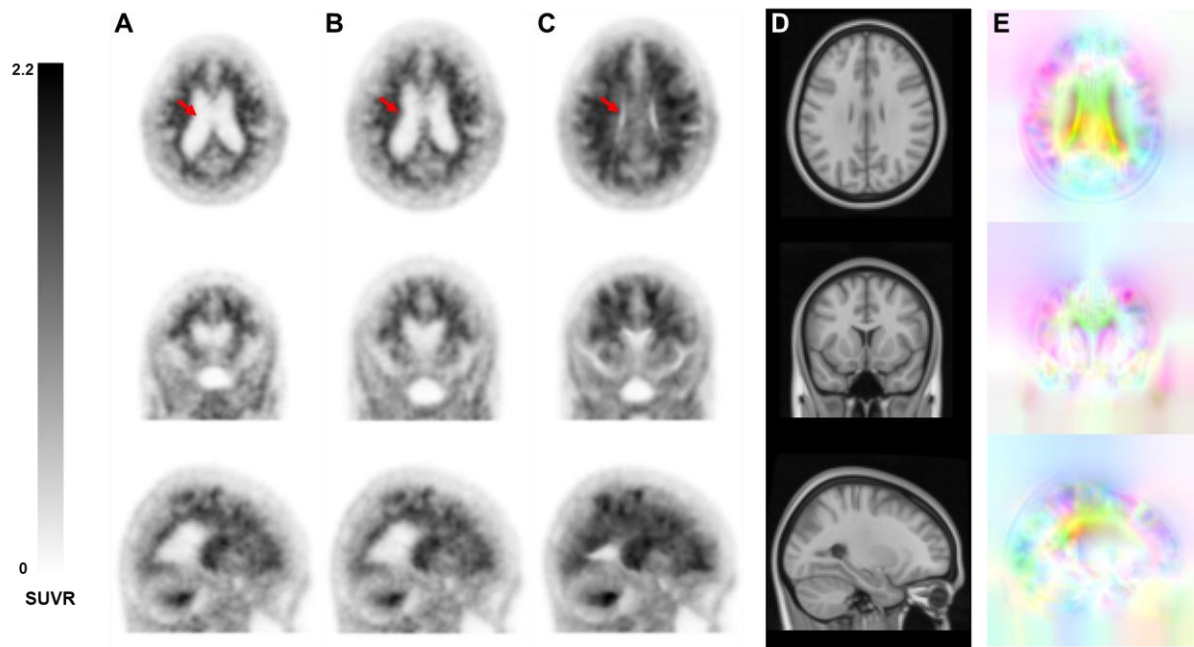


**FIGURE 2.** Spatial normalization of  $^{18}\text{F}$ -Florbetaben PET in an amyloid positive case. (A) Input image in individual space, (B) MRI-based spatially normalization using SPM12, (C) PET spatial normalization using DNN, (D) T1 MRI template, and (E) estimated deformation fields using DNN (R: anteroposterior, G: longitudinal, B: mediolateral).



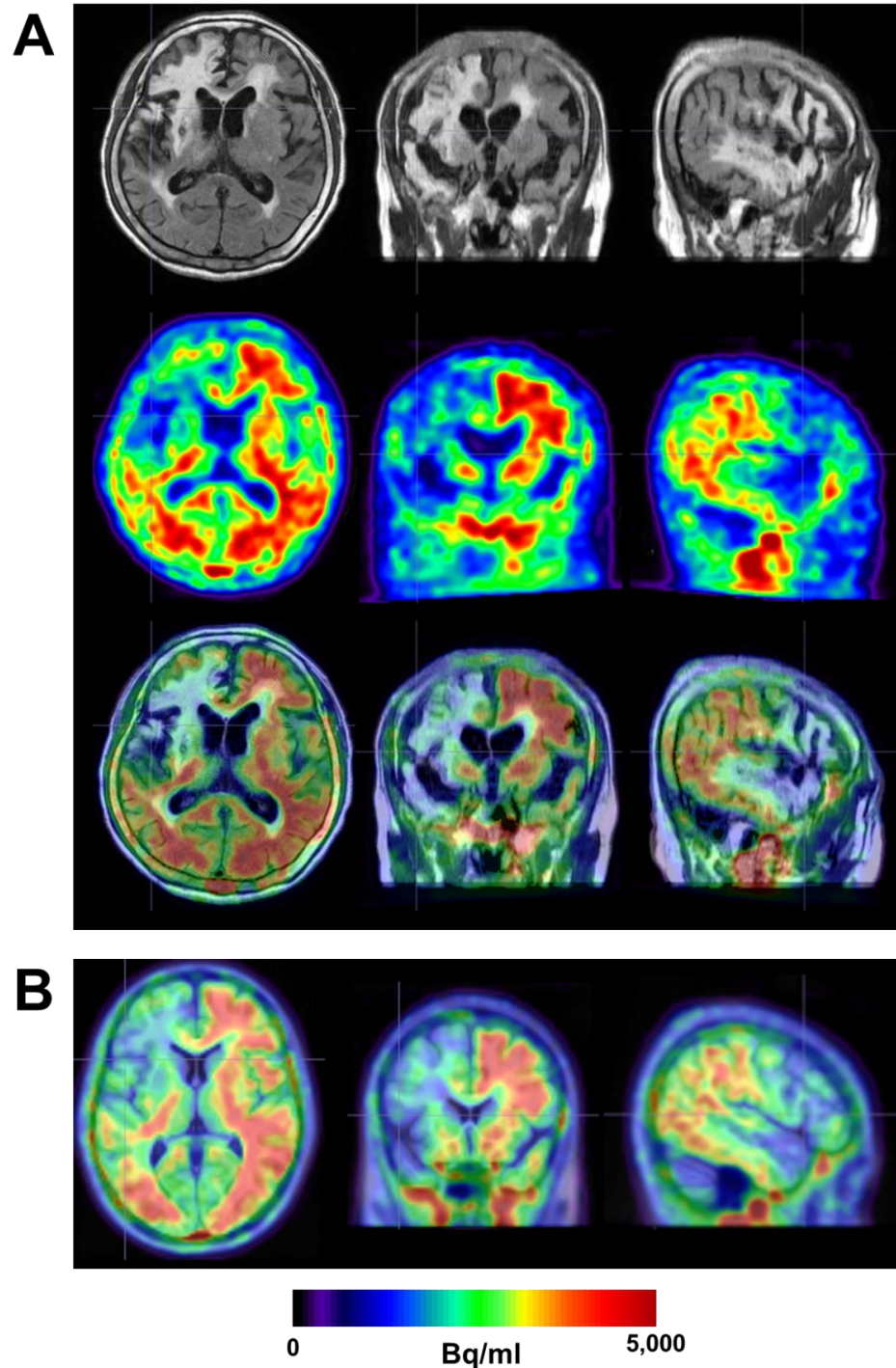


**FIGURE 3.** Spatial normalization result of a patient with chronic stroke lesion using the proposed method.

(A) Patient's original Flair MRI,  $^{18}\text{F}$ -Florbetaben and PET/MRI fusion. (B) SN PET overlaid on standard T1 MRI template.

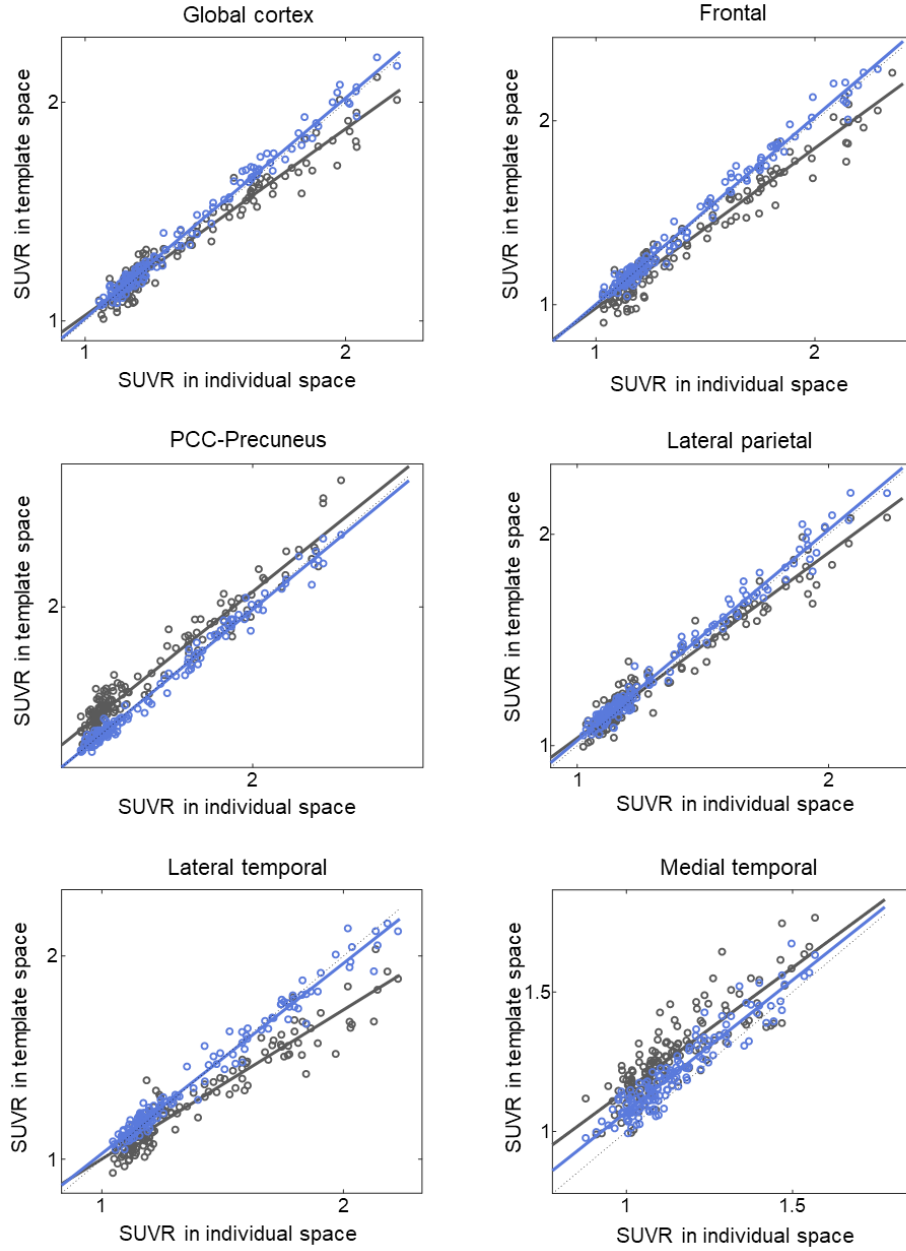


**FIGURE 4.** Internal validation: SUVR comparison in  $^{18}\text{F}$ -Florbetaben and  $^{18}\text{F}$ -Flutemetamol ( $n=148$ ). The  $X$ -axis represents the ground truth SUVR estimated in an individual space using FreeSurfer VOI, whereas the  $Y$ -axis represents the SUVR estimated in a template space using co-registered MRI and SPM12 (black symbols and lines) or the proposed DNN (sky blue symbols and lines).

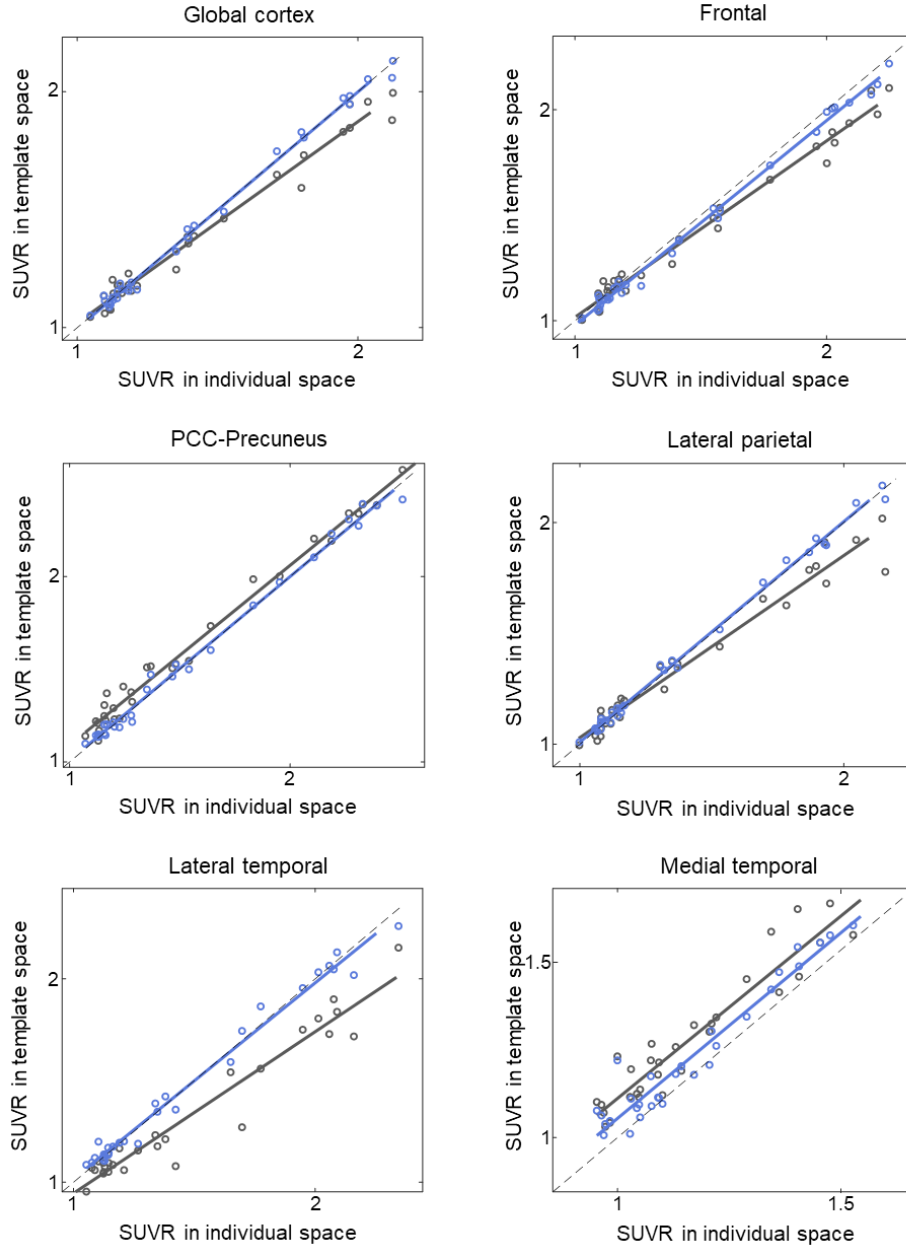


**FIGURE 5.** External validation: SUVR comparison in  $^{18}\text{F}$ -Florbetaben ( $n=30$ ). The  $X$ -axis represents the ground truth SUVR estimated in an individual space using FreeSurfer VOI, whereas the  $Y$ -axis represents the SUVR estimated in a template space using co-registered MRI and SPM12 (black symbols and lines) or the proposed DNN (sky blue symbols and lines).

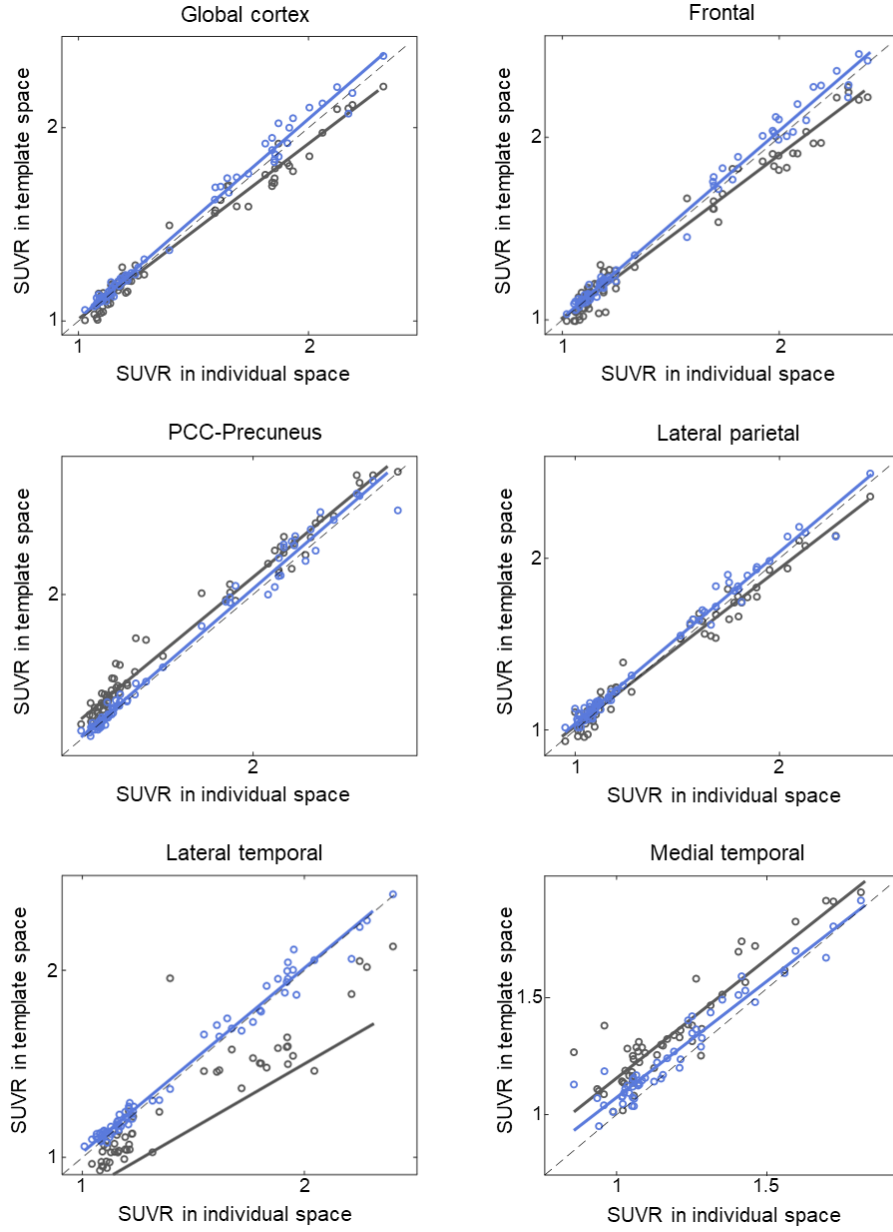


**FIGURE 6.** External validation: SUVR comparison in  $^{18}\text{F}$ -Flutemetamol ( $n=67$ ). The  $X$ -axis represents the ground truth SUVR estimated in an individual space using FreeSurfer VOI, whereas the  $Y$ -axis represents the SUVR estimated in a template space using co-registered MRI and SPM12 (black symbols and lines) or the proposed DNN (sky blue symbols and lines).

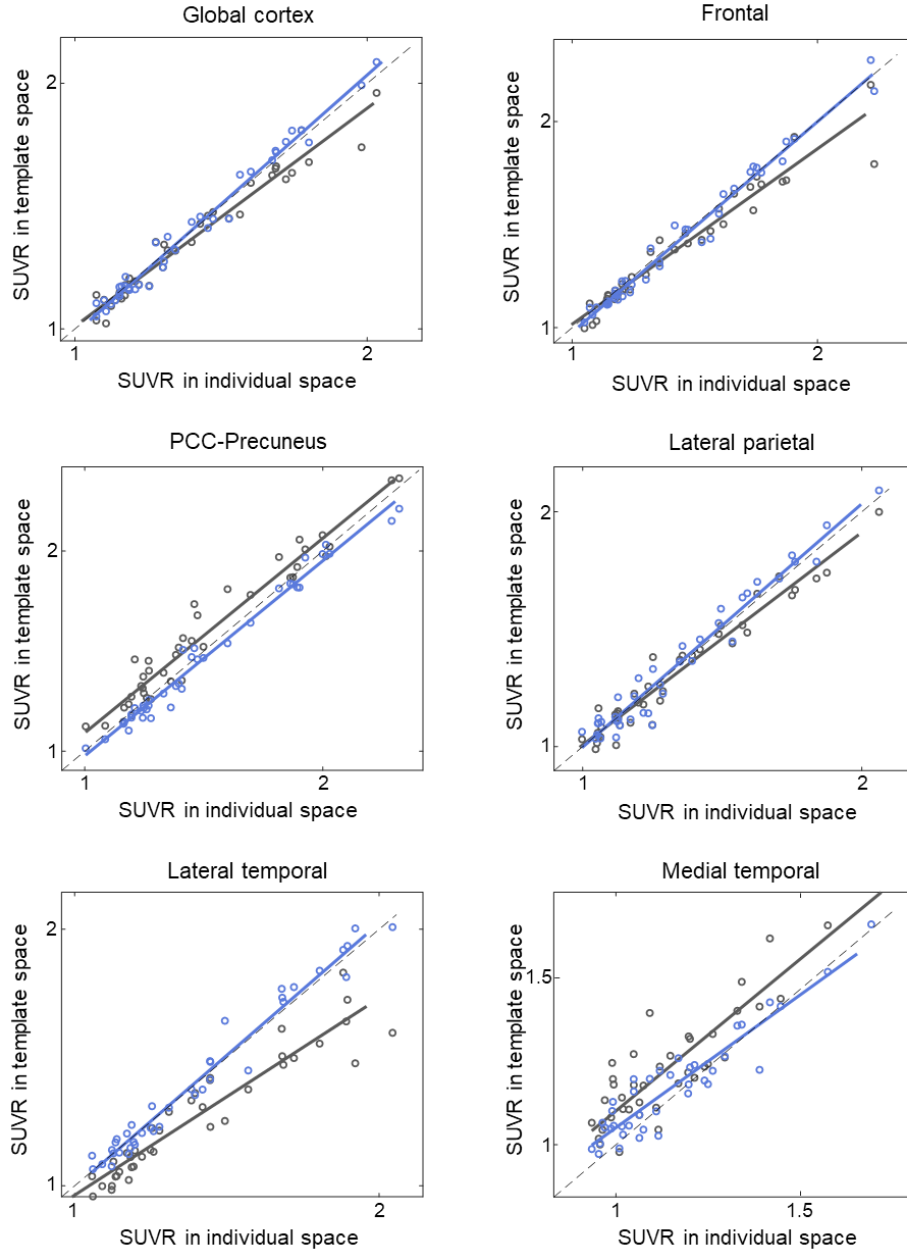


**FIGURE 7.** External validation: SUVR comparison in  $^{18}\text{F}$ -Florbetapir ( $n=39$ ). The X-axis represents the ground truth SUVR estimated in an individual space using FreeSurfer VOI, whereas the Y-axis represents the SUVR estimated in a template space using co-registered MRI and SPM12 (black symbols and lines) or the proposed DNN (sky blue symbols and lines).

## REFERENCES

1. Kwon JS, Kim JJ, Lee DW, et al. Neural correlates of clinical symptoms and cognitive dysfunctions in obsessive-compulsive disorder. *Psychiatry Res.* 2003;122:37-47.
2. Lee DS, Lee JS, Oh SH, et al. Deafness: cross-modal plasticity and cochlear implants. *Nature.* 2001;409:149-150.
3. Nordberg A, Rinne JO, Kadir A, Långström B. The use of PET in Alzheimer disease. *Nat Rev Neurol.* 2010;6:78-87.
4. Rowe CC, Ng S, Ackermann U, et al. Imaging  $\beta$ -amyloid burden in aging and dementia. *J Neurol.* 2007;68:1718-1725.
5. Oh M, Kim JS, Kim JY, et al. Subregional patterns of preferential striatal dopamine transporter loss differ in Parkinson disease, progressive supranuclear palsy, and multiple-system atrophy. *J Nucl Med.* 2012;53:399-406.
6. Wong DF, Rosenberg PB, Zhou Y, et al. In vivo imaging of amyloid deposition in Alzheimer disease using the radioligand 18F-AV-45 (Flobetapir). *J Nucl Med.* 2010;51:913.
7. Choi H, Cheon GJ, Kim HJ, et al. Gray matter correlates of dopaminergic degeneration in Parkinson's disease: A hybrid PET/MR study using (18) F-FP-CIT. *Hum Brain Mapp.* 2016;37:1710-1721.
8. Small Gary W, Ercoli Linda M, Silverman Daniel HS, et al. Cerebral metabolic and cognitive decline in persons at genetic risk for Alzheimer's disease. *Proc Natl Acad Sci U S A* 2000;97:6037-6042.
9. Förster S, Grimmer T, Miederer I, et al. Regional expansion of hypometabolism in Alzheimer's disease follows amyloid deposition with temporal delay. *Biol Psychiatry.* 2012;71:792-797.
10. Ashburner J, Friston KJ. Nonlinear spatial normalization using basis functions. *Hum brain Mapp.* 1999;7:254-266.
11. Lancaster JL, Glass TG, Lankipalli BR, Downs H, Mayberg H, Fox PT. A modality-independent approach to spatial normalization of tomographic images of the human brain. *Hum Brain Mapp.* 1995;3:209-223.
12. Minoshima S, Koeppe RA, Frey KA, Kuhl DE. Anatomic standardization: linear scaling and

nonlinear warping of functional brain images. *J Nucl Med*. 1994;35:1528-1537.

**13.** Kang KW, Lee DS, Cho JH, et al. Quantification of F-18 FDG PET images in temporal lobe epilepsy patients using probabilistic brain atlas. *Neuroimage*. 2001;14:1-6.

**14.** Lee JS, Lee DS, Kim S-K, et al. Localization of epileptogenic zones in F-18 FDG brain PET of patients with temporal lobe epilepsy using artificial neural network. *IEEE Trans Med Imaging*. 2000;19:347-355.

**15.** Evans AC, Janke AL, Collins DL, Baillet S. Brain templates and atlases. *Neuroimage*. 2012;62:911-922.

**16.** Caviness VS, Meyer J, Makris N, Kennedy DN, Jernigan JC. MRI-based topographic parcellation of human neocortex: an anatomically specified method with estimate of reliability. *J Cogn Neurosci*. 1996;8:566-587.

**17.** Eickhoff SB, Stephan KE, Mohlberg H, et al. A new SPM toolbox for combining probabilistic cytoarchitectonic maps and functional imaging data. *NeuroImage*. 2005;25:1325-1335.

**18.** Tzourio-Mazoyer N, Landeau B, Papathanassiou D, et al. Automated anatomical labeling of activations in SPM using a macroscopic anatomical parcellation of the MNI MRI single-subject brain. *NeuroImage*. 2002;15:273-289.

**19.** Lee JS, Lee DS. Analysis of functional brain images using population-based probabilistic atlas. *Curr Med Imaging Review*. 2005;1:81-87.

**20.** Mintun MA, Lo AC, Duggan Evans C, et al. Donanemab in Early Alzheimer's Disease. *N Engl J Med*. 2021;384:1691-1704.

**21.** Sevigny J, Chiao P, Bussière T, et al. The antibody aducanumab reduces A $\beta$  plaques in Alzheimer's disease. *Nature*. 2016;537:50-56.

**22.** Barthel H, Gertz H-J, Dresel S, et al. Cerebral amyloid- $\beta$  PET with florbetaben (18 F) in patients with Alzheimer's disease and healthy controls: a multicentre phase 2 diagnostic study. *The Lancet Neurology*. 2011;10:424-435.

**23.** Klein A, Andersson J, Ardekani BA, et al. Evaluation of 14 nonlinear deformation algorithms applied to human brain MRI registration. *Neuroimage*. 2009;46:786-802.

24. Klunk WE, Engler H, Nordberg A, et al. Imaging brain amyloid in Alzheimer's disease with Pittsburgh Compound-B. *Ann Neurol*. 2004;55:306-319.
25. Choi H, Lee DS. Generation of structural MR images from amyloid PET: application to MR-less quantification. *J Nucl Med*. 2018;59:1111-1117.
26. Kang SK, Seo S, Shin SA, et al. Adaptive template generation for amyloid PET using a deep learning approach. *Hum Brain Mapp*. 2018;39:3769-3778.
27. Ashburner J, Friston KJ. Unified segmentation. *Neuroimage*. 2005;26:839-851.
28. Fischl B. FreeSurfer. *NeuroImage*. 2012;62:774-781.
29. Clerx L, Gronenschild EH, Echavarri C, Verhey F, Aalten P, Jacobs HI. Can freeSurfer compete with manual volumetric measurements in Alzheimer's disease? *Curr Alzheimer Res*. 2015;12:358-367.
30. Kuperberg GR, Broome MR, McGuire PK, et al. Regionally localized thinning of the cerebral cortex in schizophrenia. *Arch Gen Psychiatry*. 2003;60:878-888.
31. Salat DH, Buckner RL, Snyder AZ, et al. Thinning of the cerebral cortex in aging. *Cereb Cortex*. 2004;14:721-730.
32. Su Y, D'Angelo GM, Vlassenko AG, et al. Quantitative analysis of PiB-PET with FreeSurfer ROIs. *PLoS One*. 2013;8:e73377.
33. Tuszynski T, Rullmann M, Luthardt J, et al. Evaluation of software tools for automated identification of neuroanatomical structures in quantitative  $\beta$ -amyloid PET imaging to diagnose Alzheimer's disease. *Eur J Nucl Med Mol Imaging*. 2016;43:1077-1087.
34. Rowe CC, Doré V, Jones G, et al. 18F-Florbetaben PET beta-amyloid binding expressed in Centiloids. *Eur J Nucl Med Mol Imaging*. 2017;44:2053-2059.
35. Battle MR, Pillay LC, Lowe VJ, et al. Centiloid scaling for quantification of brain amyloid with [18F]flutemetamol using multiple processing methods. *EJNMMI Research*. 2018;8:107.
36. Navitsky M, Joshi AD, Kennedy I, et al. Standardization of amyloid quantitation with florbetapir standardized uptake value ratios to the Centiloid scale. *Alzheimers Dement*. 2018;14:1565-1571.



- 37.** Ronneberger O, Fischer P, Brox T. U-net: Convolutional networks for biomedical image segmentation. Paper presented at: International Conference on Medical image computing and computer-assisted intervention, 2015.
- 38.** Fonov V, Evans AC, Botteron K, et al. Unbiased average age-appropriate atlases for pediatric studies. *Neuroimage*. 2011;54:313-327.
- 39.** Fonov VS, Evans AC, McKinstry RC, Almli C, Collins D. Unbiased nonlinear average age-appropriate brain templates from birth to adulthood. *NeuroImage*. 2009:S102.
- 40.** Ripollés P, Marco-Pallarés J, de Diego-Balaguer R, et al. Analysis of automated methods for spatial normalization of lesioned brains. *Neuroimage*. 2012;60:1296-1306.
- 41.** Kim JY, Oh D, Sung K, et al. Visual interpretation of [(18)F]Florbetaben PET supported by deep learning-based estimation of amyloid burden. *Eur J Nucl Med Mol Imaging*. 2021;48:1116-1123.
- 42.** Kim JY, Suh HY, Ryoo HG, et al. Amyloid PET quantification via end-to-end training of a deep learning. *Nucl Med Mol Imaging*. 2019;53:340-348.

**TABLE 1.** Demographic and clinical diagnosis of the training and test datasets

	<b><i>n</i></b>	<b>Age</b>	<b>Sex (M/F)</b>	<b>Diagnosis (NC/MCI/AD)</b>	<b>Tracer (FMM/FBB)</b>
Training set	994	73.2 $\pm$ 5.6	318/676	200/543/251	367/627
Test set	148	74.8 $\pm$ 6.6	75/73	26/85/37	64/84

NC, normal control; MCI, mild cognitive impairment; AD, Alzheimer's disease; FMM,  $^{18}\text{F}$ -Flutemetamol; FBB,  $^{18}\text{F}$ -Florbetaben

**TABLE 2.** Demographic and clinical diagnosis of the external test dataset

<b>Tracer</b>	<b><i>n</i></b>	<b>Age</b>	<b>Sex (M/F)</b>	<b>Diagnosis (YC/Elderly)</b>
<sup>18</sup> F-Florbetaben	30			8/22
<sup>18</sup> F-Flutemetamol	67	Anonymized	Anonymized	22/45
<sup>18</sup> F-Florbetapir	39			12/27

YC: young control

**TABLE 3.** Internal validation: Pearson’s correlation and ICC analysis for SUVR of the internal  $^{18}\text{F}$ -Florbetaben and  $^{18}\text{F}$ -Flutemetamol dataset ( $n=148$ ) relative to the FreeSurfer approach

Internal dataset	SPM				Proposed			
	Slope	$y$ -intercept	$R^2$	ICC	Slope	$y$ -intercept	$R^2$	ICC
Global	0.869	0.113	0.946	0.965	<b>1.019</b>	<b>-0.016</b>	<b>0.986</b>	<b>0.992</b>
Frontal	0.956	0.183	0.947	0.946	<b>0.983</b>	<b>0.019</b>	<b>0.987</b>	<b>0.992</b>
PCC-Precuneus	0.877	0.158	0.950	0.921	<b>0.998</b>	<b>0.026</b>	<b>0.981</b>	<b>0.993</b>
Lateral parietal	0.734	0.267	0.910	0.970	<b>0.936</b>	<b>0.092</b>	<b>0.977</b>	<b>0.988</b>
Lateral temporal	0.853	0.173	0.957	0.865	<b>1.008</b>	<b>0.003</b>	<b>0.987</b>	<b>0.987</b>
Medial temporal	0.879	0.269	0.732	0.554	<b>0.944</b>	<b>0.125</b>	<b>0.891</b>	<b>0.861</b>

**TABLE 4.** External validation: Pearson’s correlation and ICC analysis for SUVR of the external  $^{18}\text{F}$ -Florbetaben dataset ( $n=30$ ) relative to the FreeSurfer approach

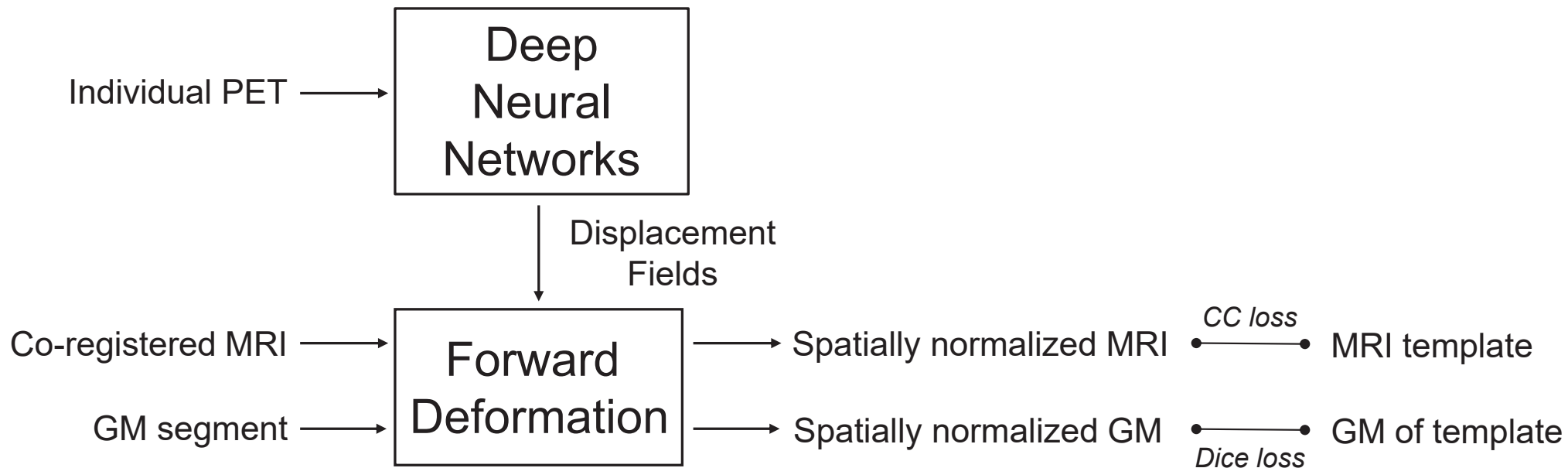
$^{18}\text{F}$ -FBB	SPM				Proposed			
	Slope	$y$ -intercept	$R^2$	ICC	Slope	$y$ -intercept	$R^2$	ICC
Global	0.853	0.167	0.979	0.972	<b>1.003</b>	<b>-0.006</b>	<b>0.995</b>	<b>0.998</b>
Frontal	0.836	0.181	0.983	0.966	<b>0.970</b>	<b>0.010</b>	<b>0.995</b>	<b>0.994</b>
PCC-Precuneus	0.970	0.121	0.986	0.981	<b>0.990</b>	<b>0.019</b>	<b>0.993</b>	<b>0.996</b>
Lateral parietal	0.821	0.209	0.965	0.961	<b>0.994</b>	<b>0.016</b>	<b>0.996</b>	<b>0.998</b>
Lateral temporal	0.794	0.151	0.936	0.879	<b>0.963</b>	<b>0.054</b>	<b>0.986</b>	<b>0.993</b>
Medial temporal	0.972	0.134	0.898	0.800	<b>0.990</b>	<b>0.062</b>	<b>0.931</b>	<b>0.927</b>

**TABLE 5.** External validation: Pearson’s correlation and ICC analysis for SUVR of the external  $^{18}\text{F}$ -Flutemetamol ( $n=67$ ) relative to the FreeSurfer approach

$^{18}\text{F}$ -FMM	SPM				Proposed			
	Slope	$y$ -intercept	$R^2$	ICC	Slope	$y$ -intercept	$R^2$	ICC
Global	0.907	0.104	0.979	0.977	<b>1.033</b>	<b>-0.020</b>	<b>0.990</b>	<b>0.989</b>
Frontal	0.893	0.117	0.976	0.975	<b>1.025</b>	<b>-0.015</b>	<b>0.990</b>	<b>0.987</b>
PCC-Precuneus	0.978	0.150	0.978	0.945	<b>1.024</b>	<b>-0.032</b>	<b>0.985</b>	<b>0.984</b>
Lateral parietal	0.919	0.103	0.975	0.969	<b>1.001</b>	<b>0.036</b>	<b>0.987</b>	<b>0.979</b>
Lateral temporal	0.794	0.136	0.946	0.844	<b>0.986</b>	<b>0.042</b>	<b>0.984</b>	<b>0.984</b>
Medial temporal	0.943	0.206	0.857	0.758	<b>0.921</b>	<b>0.149</b>	<b>0.926</b>	<b>0.931</b>

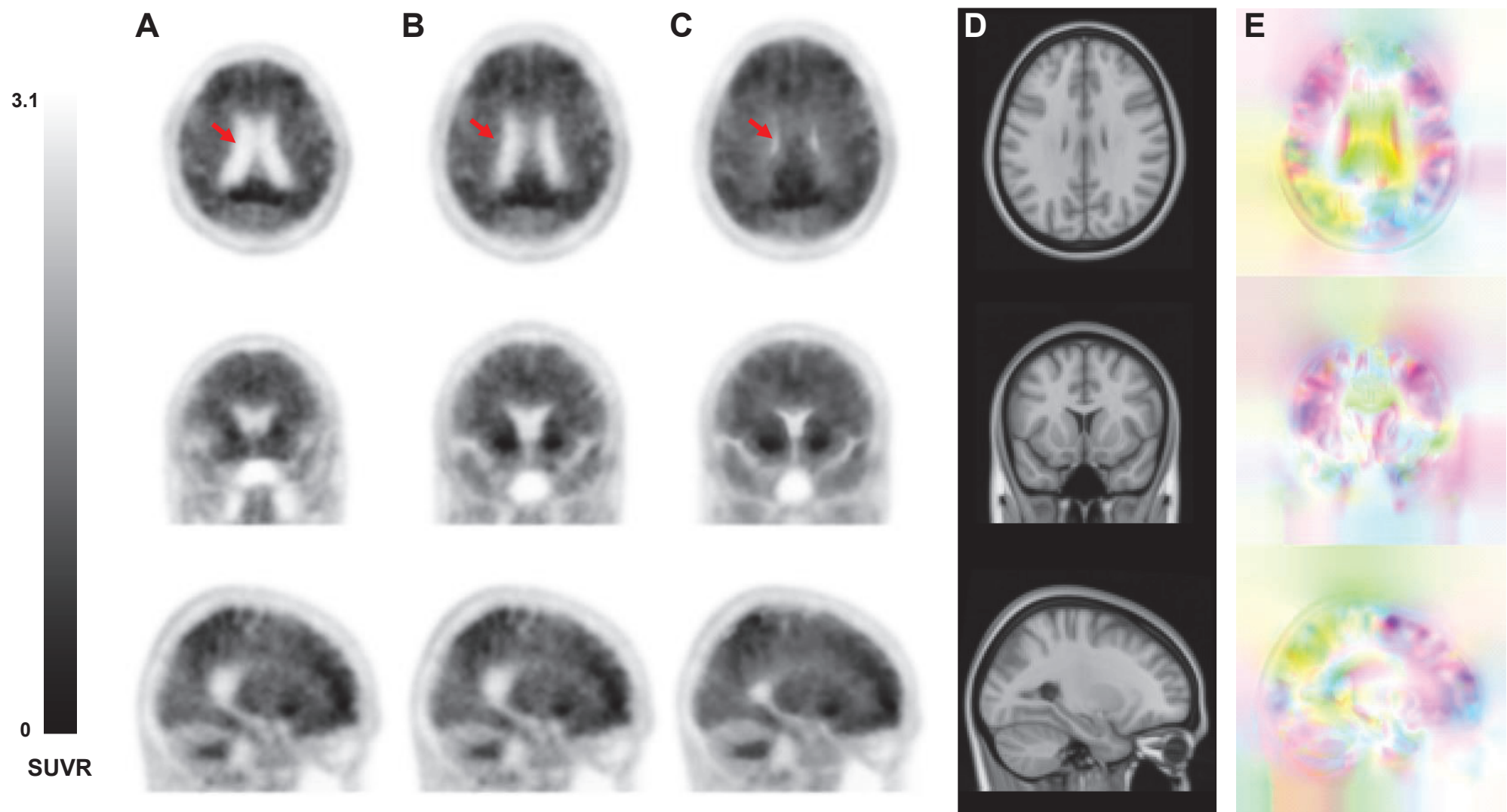
**TABLE 6.** External validation: Pearson’s correlation and ICC analysis for SUVR of the external  $^{18}\text{F}$ -Florbetapir dataset ( $n=39$ ) relative to the FreeSurfer approach

$^{18}\text{F}$ -FBP	SPM				Proposed			
	Slope	$y$ -intercept	$R^2$	ICC	Slope	$y$ -intercept	$R^2$	ICC
Global	0.888	0.123	0.961	0.979	<b>1.082</b>	<b>-0.071</b>	<b>0.982</b>	<b>0.985</b>
Frontal	0.851	0.166	0.940	0.974	<b>1.022</b>	<b>-0.045</b>	<b>0.980</b>	<b>0.989</b>
PCC-Precuneus	0.973	0.119	0.948	0.940	<b>0.975</b>	<b>0.001</b>	<b>0.980</b>	<b>0.982</b>
Lateral parietal	0.905	0.102	0.949	<b>0.981</b>	<b>1.037</b>	<b>-0.039</b>	<b>0.958</b>	0.978
Lateral temporal	0.768	0.196	0.892	0.854	<b>1.029</b>	<b>-0.034</b>	<b>0.970</b>	<b>0.990</b>
Medial temporal	<b>0.977</b>	<b>0.128</b>	0.798	0.742	0.855	0.199	<b>0.864</b>	<b>0.936</b>

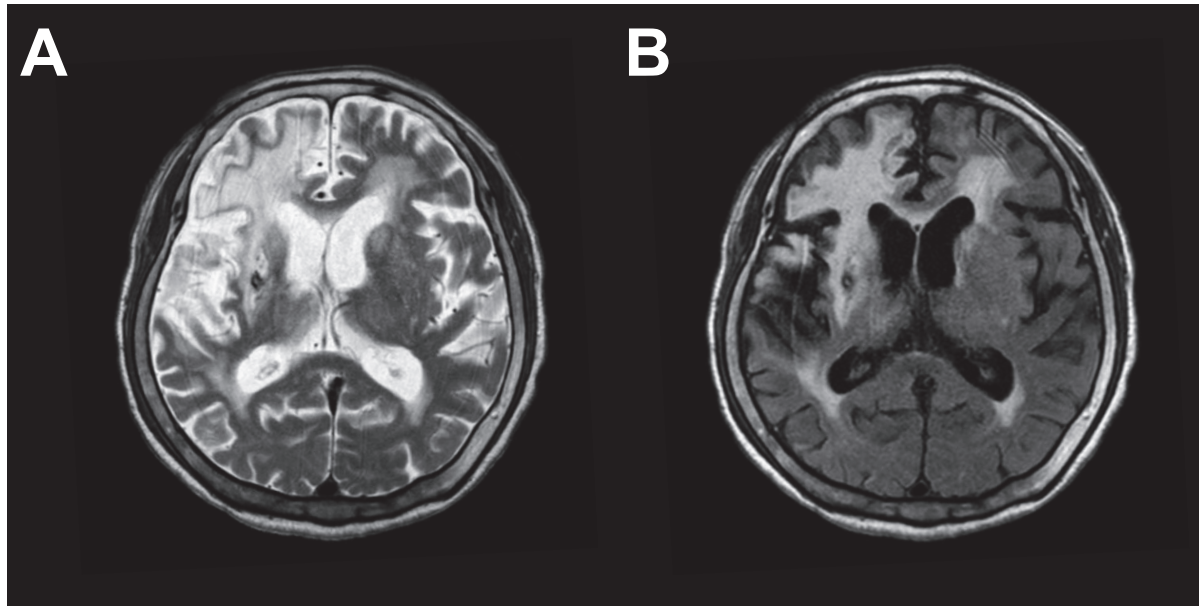


**SUPPLEMENTAL FIGURE 1.** Schematic of deep neural network training (GM: gray matter, CC: cross-correlation).

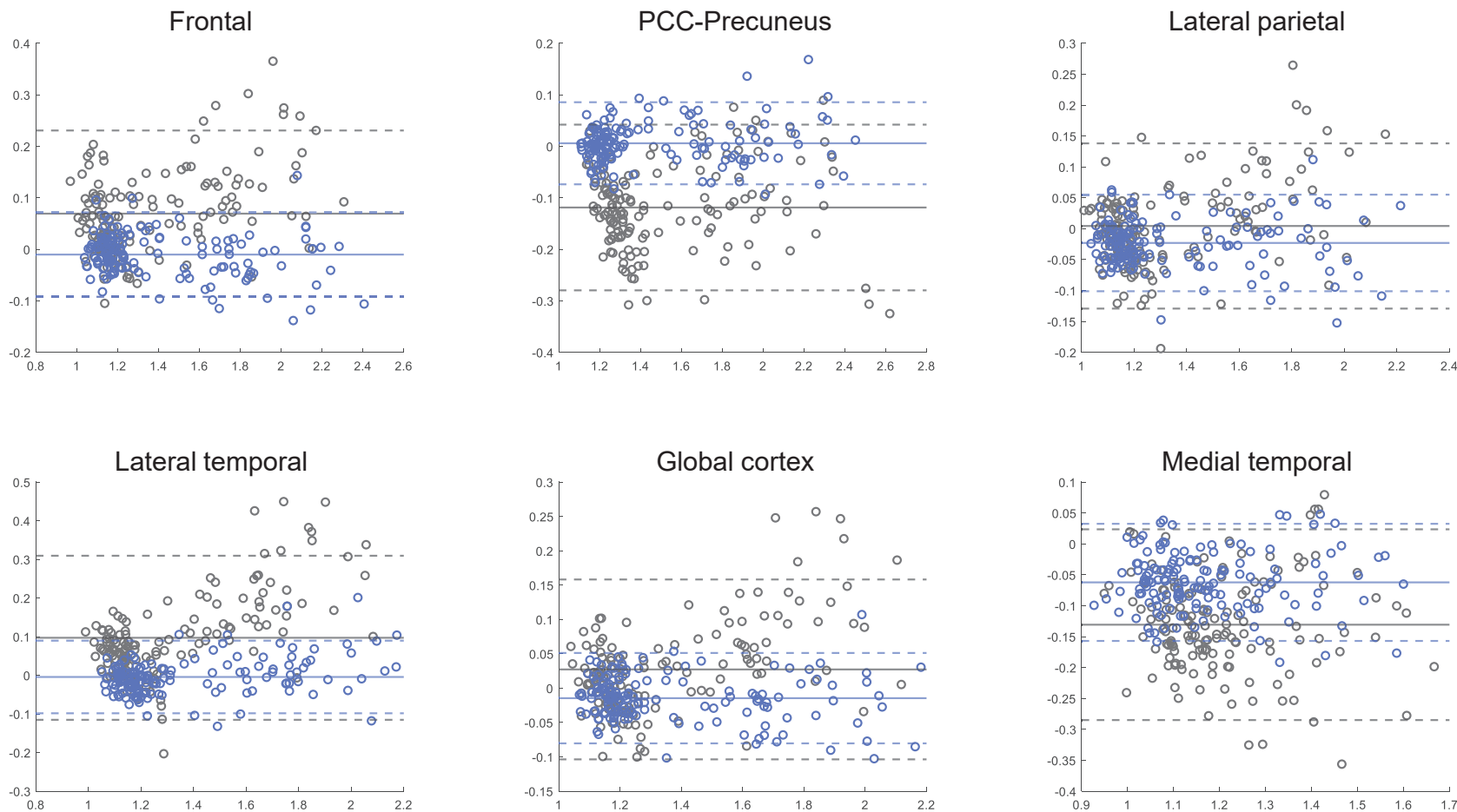




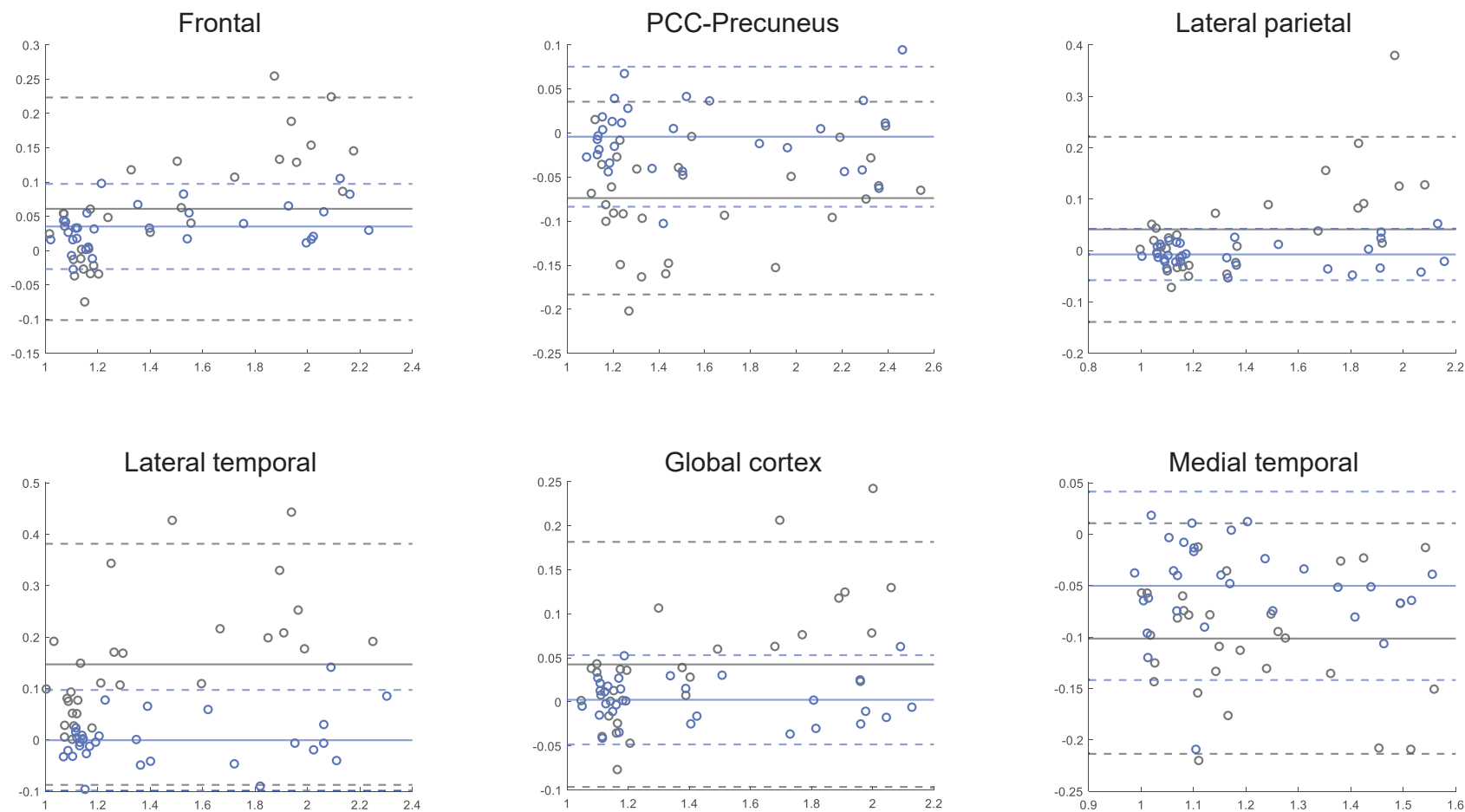
**SUPPLEMENTAL FIGURE 2.** Spatial normalization of  $^{18}\text{F}$ -Florbetaben PET in an amyloid-negative case. (A) Input image in individual space. (B) MRI-based spatial normalization using SPM12. (C) PET spatial normalization using a DNN. (D) T1 MRI template. (E) Deformation fields estimated using DNN (R: anteroposterior, G: longitudinal, B: mediolateral).



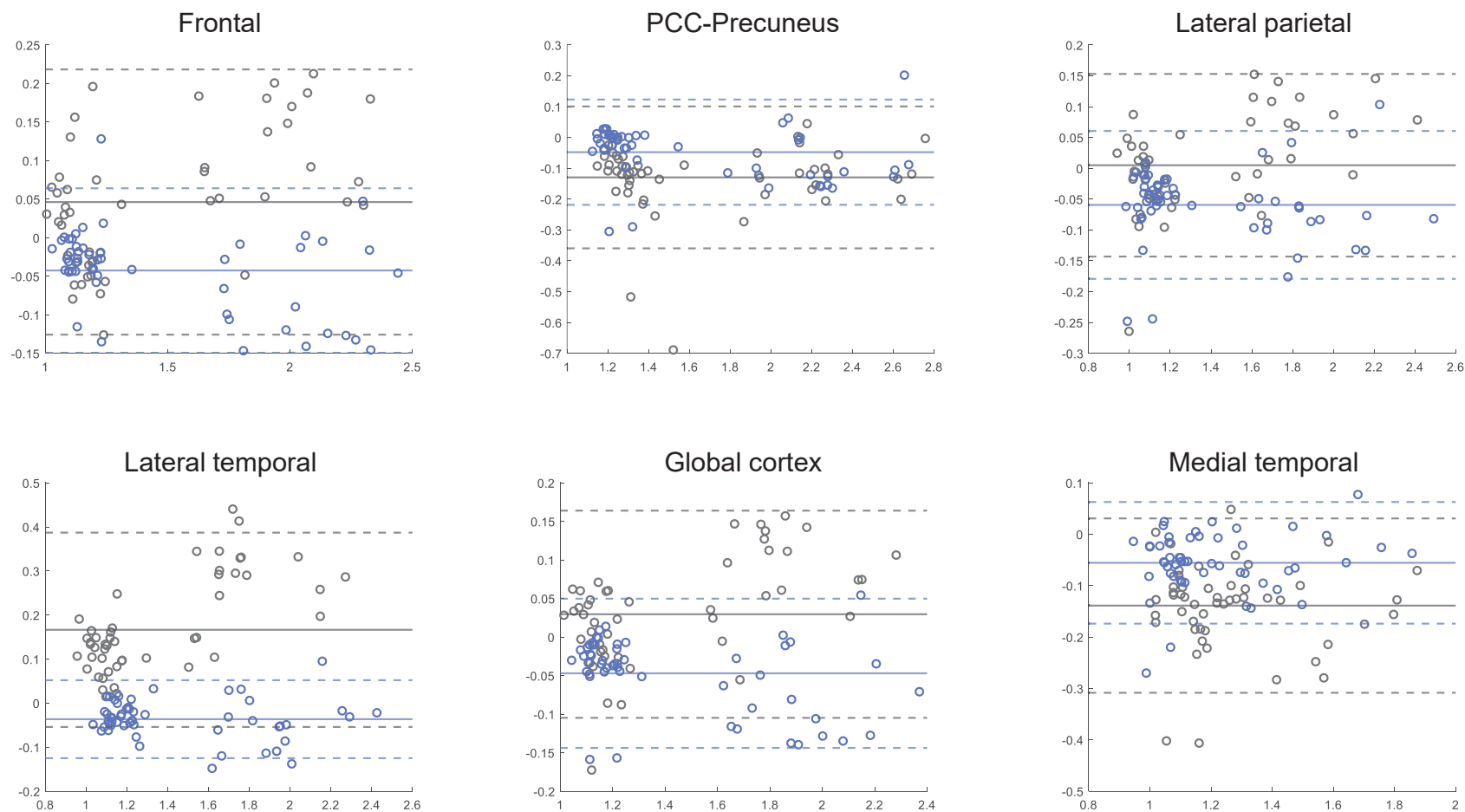
**SUPPLEMENTAL FIGURE 3.** A patient with chronic stroke lesion. (A) T2 and (B) FLAIR MRI.



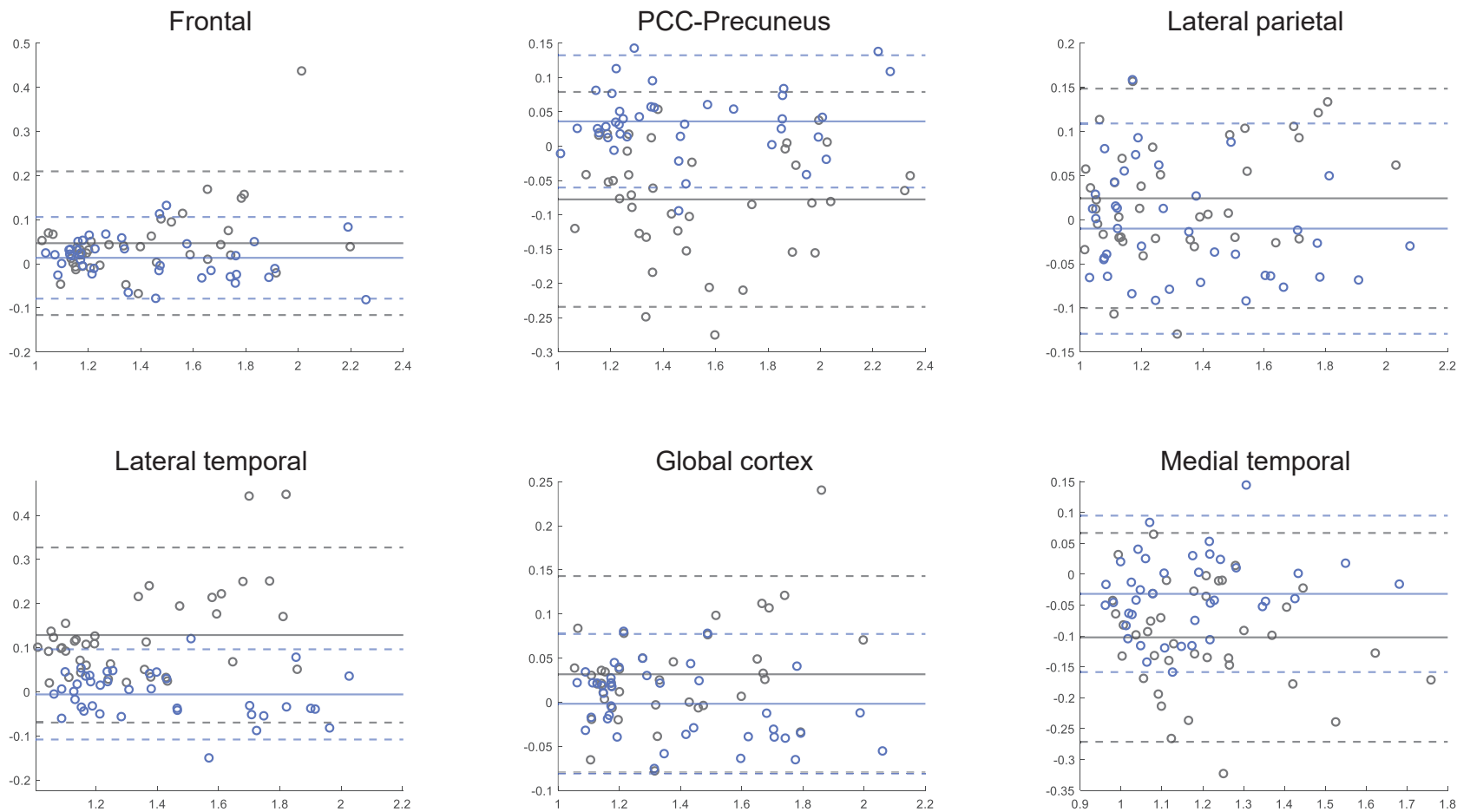
**SUPPLEMENTAL FIGURE 4.** Internal validation: Bland-Altman analysis of SUVR values obtained using the FreeSurfer approach and spatial normalization techniques (SPM12 or DNN) from the internal  $^{18}\text{F}$ -Florbetaben and  $^{18}\text{F}$ -Flutemetamol dataset ( $n=148$ ). SPM12: Black symbols and lines. DNN: sky blue symbols and lines.



**SUPPLEMENTAL FIGURE 5.** External validation: Bland-Altman analysis of SUVR values obtained using the FreeSurfer approach and spatial normalization techniques (SPM12 or DNN) from external  $^{18}\text{F}$ -Florbetaben ( $n=30$ ). SPM12: Black symbols and lines. DNN: sky blue symbols and lines.



**SUPPLEMENTAL FIGURE 6.** External validation: Bland-Altman analysis of SUVR values obtained using the FreeSurfer approach and spatial normalization techniques (SPM12 or DNN) from the external  $^{18}\text{F}$ -Flutemetamol dataset ( $n=67$ ). SPM12: Black symbols and lines. DNN: sky blue symbols and lines.



**SUPPLEMENTAL FIGURE 7.** External validation: Bland-Altman analysis of SUVR values obtained using the FreeSurfer approach and spatial normalization techniques (SPM12 or DNN) from the external  $^{18}\text{F}$ -Florbetapir dataset ( $n=39$ ). SPM12: Black symbols and lines. DNN: sky blue symbols and lines.

**Supplementary TABLE 1.** Internal validation: Pearson's correlation and ICC analysis for SUVR of the internal  $^{18}\text{F}$ -Florbetaben and  $^{18}\text{F}$ -Flutemetamol dataset ( $n=148$ ) relative to the FreeSurfer approach

Negative

Internal negative ( $n=107$ )	SPM				Proposed			
	Slope	y-intercept	$R^2$	ICC	Slope	y-intercept	$R^2$	ICC
Global	0.921	0.091	0.796	0.894	0.969	0.049	0.913	0.950
Frontal	0.961	0.005	0.779	0.833	0.994	0.012	0.922	0.960
PCC-Precuneus	0.951	0.191	0.790	0.583	0.901	0.119	0.941	0.967
Lateral parietal	0.908	0.122	0.711	0.833	0.943	0.088	0.870	0.907
Lateral temporal	0.840	0.141	0.724	0.771	0.88	0.156	0.902	0.943
Medial temporal	1.005	0.135	0.550	0.007	0.801	0.273	0.662	0.527

Positive

Internal positive ( $n=41$ )	SPM				Proposed			
	Slope	y-intercept	$R^2$	ICC	Slope	y-intercept	$R^2$	ICC
Global	0.809	0.251	0.820	0.777	0.946	0.119	0.940	0.962
Frontal	0.880	0.086	0.841	0.731	0.965	0.090	0.940	0.964
PCC-Precuneus	1.006	0.081	0.826	0.841	0.931	0.131	0.945	0.972
Lateral parietal	0.842	0.220	0.837	0.875	0.958	0.101	0.924	0.954
Lateral temporal	0.699	0.327	0.698	0.343	0.845	0.266	0.890	0.937
Medial temporal	0.806	0.363	0.457	0.444	0.820	0.304	0.737	0.727

**Supplementary TABLE 2.** External validation: Pearson's correlation and ICC analysis for SUVR of the external  $^{18}\text{F}$ -Florbetaben dataset ( $n=30$ ) relative to the FreeSurfer approach

Negative

$^{18}\text{F}$ -FBB negative ( $n=20$ )	SPM				Proposed			
	Slope	y-intercept	$R^2$	ICC	Slope	y-intercept	$R^2$	ICC
Global	0.841	0.181	0.864	0.926	0.99	0.008	0.956	0.978
Frontal	0.859	0.156	0.914	0.949	0.931	0.056	0.966	0.966
PCC-Precuneus	0.941	0.153	0.818	0.757	0.986	0.024	0.923	0.961
Lateral parietal	1.001	0.003	0.889	0.944	1.016	-0.010	0.967	0.981
Lateral temporal	0.444	0.566	0.412	0.290	0.894	0.132	0.876	0.936
Medial temporal	0.932	0.176	0.712	0.333	0.620	0.447	0.538	0.590

Positive

$^{18}\text{F}$ -FBB positive ( $n=10$ )	SPM				Proposed			
	Slope	y-intercept	$R^2$	ICC	Slope	y-intercept	$R^2$	ICC
Global	0.860	0.154	0.873	0.771	0.975	0.049	0.973	0.988
Frontal	0.942	-0.038	0.935	0.719	1.006	-0.062	0.976	0.960
PCC-Precuneus	0.900	0.276	0.976	0.958	0.98	0.042	0.970	0.987
Lateral parietal	0.724	0.393	0.721	0.638	0.964	0.074	0.967	0.984
Lateral temporal	0.962	-0.179	0.785	0.437	0.845	0.296	0.903	0.948
Medial temporal	0.999	0.098	0.721	0.636	1.013	0.044	0.970	0.869



**Supplementary TABLE 3.** External validation: Pearson's correlation and ICC analysis for SUVR of the external  $^{18}\text{F}$ -Flutemetamol ( $n=67$ ) relative to the FreeSurfer approach

Negative

$^{18}\text{F}$ -FMM negative ( $n=43$ )	SPM				Proposed			
	Slope	y-intercept	$R^2$	ICC	Slope	y-intercept	$R^2$	ICC
Global	1.196	-0.228	0.813	0.869	0.947	0.075	0.926	0.941
Frontal	1.145	-0.171	0.774	0.853	0.832	0.203	0.902	0.936
PCC-Precuneus	1.374	-0.343	0.772	0.364	1.065	-0.069	0.914	0.942
Lateral parietal	1.167	-0.168	0.711	0.790	0.890	0.154	0.804	0.784
Lateral temporal	1.023	-0.127	0.705	0.375	0.839	0.207	0.855	0.887
Medial temporal	0.950	0.182	0.455	-0.073	0.724	0.325	0.643	0.687

Positive

$^{18}\text{F}$ -FMM positive ( $n=24$ )	SPM				Proposed			
	Slope	y-intercept	$R^2$	ICC	Slope	y-intercept	$R^2$	ICC
Global	0.879	0.155	0.895	0.879	0.933	0.173	0.913	0.928
Frontal	0.881	0.138	0.887	0.843	0.95	0.144	0.927	0.945
PCC-Precuneus	0.913	0.294	0.910	0.877	0.876	0.323	0.859	0.909
Lateral parietal	0.876	0.181	0.912	0.934	0.929	0.173	0.925	0.945
Lateral temporal	0.806	0.108	0.765	0.365	0.879	0.253	0.895	0.940
Medial temporal	1.023	0.091	0.845	0.735	0.827	0.278	0.895	0.919

**Supplementary TABLE 4.** External validation: Pearson's correlation and ICC analysis for SUVR of the external  $^{18}\text{F}$ -Florbetapir dataset ( $n=39$ ) relative to the FreeSurfer approach

Negative

$^{18}\text{F}$ -FBP negative ( $n=27$ )	SPM				Proposed			
	Slope	y-intercept	$R^2$	ICC	Slope	y-intercept	$R^2$	ICC
Global	1.027	-0.045	0.913	0.950	1.001	-0.009	0.911	0.953
Frontal	0.963	0.027	0.936	0.960	0.957	0.035	0.92	0.952
PCC-Precuneus	1.186	-0.153	0.795	0.731	0.999	-0.032	0.888	0.916
Lateral parietal	0.975	0.021	0.785	0.884	0.923	0.091	0.757	0.873
Lateral temporal	1.034	-0.126	0.874	0.743	0.949	0.059	0.911	0.956
Medial temporal	0.810	0.311	0.375	0.214	0.705	0.355	0.503	0.609

Positive

$^{18}\text{F}$ -FBP positive ( $n=12$ )	SPM				Proposed			
	Slope	y-intercept	$R^2$	ICC	Slope	y-intercept	$R^2$	ICC
Global	0.808	0.257	0.788	0.772	1.058	-0.078	0.937	0.957
Frontal	0.755	0.339	0.693	0.723	1.031	-0.056	0.941	0.971
PCC-Precuneus	0.928	0.197	0.887	0.903	0.852	0.249	0.923	0.927
Lateral parietal	0.851	0.193	0.885	0.881	0.972	0.080	0.910	0.940
Lateral temporal	0.673	0.353	0.498	0.128	0.885	0.231	0.798	0.887
Medial temporal	1.306	-0.331	0.893	0.806	0.908	0.130	0.833	0.919